

Thermochemistry and Accurate Quantum Reaction Rate Calculations for $\text{H}_2/\text{HD}/\text{D}_2 + \text{CH}_3^\dagger$ Gunnar Nyman,[§] Rob van Harrevelt,[‡] and Uwe Manthe**Theoretische Chemie, Fakultät für Chemie, Universität Bielefeld, Universitätsstrasse 25, 33615 Bielefeld, Germany**Received: March 8, 2007; In Final Form: April 16, 2007*

Accurate quantum-mechanical results for thermodynamic data, cumulative reaction probabilities (for $J = 0$), thermal rate constants, and kinetic isotope effects for the three isotopic reactions $\text{H}_2 + \text{CH}_3 \rightarrow \text{CH}_4 + \text{H}$, $\text{HD} + \text{CH}_3 \rightarrow \text{CH}_4 + \text{D}$, and $\text{D}_2 + \text{CH}_3 \rightarrow \text{CH}_3\text{D} + \text{D}$ are presented. The calculations are performed using flux correlation functions and the multiconfigurational time-dependent Hartree (MCTDH) method to propagate wave packets employing a Shephard interpolated potential energy surface based on high-level ab initio calculations. The calculated exothermicity for the $\text{H}_2 + \text{CH}_3 \rightarrow \text{CH}_4 + \text{H}$ reaction agrees to within 0.2 kcal/mol with experimentally deduced values. For the $\text{H}_2 + \text{CH}_3 \rightarrow \text{CH}_4 + \text{H}$ and $\text{D}_2 + \text{CH}_3 \rightarrow \text{CH}_3\text{D} + \text{D}$ reactions, experimental rate constants from several groups are available. In comparing to these, we typically find agreement to within a factor of 2 or better. The kinetic isotope effect for the rate of the $\text{H}_2 + \text{CH}_3 \rightarrow \text{CH}_4 + \text{H}$ reaction compared to those for the $\text{HD} + \text{CH}_3 \rightarrow \text{CH}_4 + \text{D}$ and $\text{D}_2 + \text{CH}_3 \rightarrow \text{CH}_3\text{D} + \text{D}$ reactions agree with experimental results to within 25% for all data points. Transition state theory is found to predict the kinetic isotope effect accurately when the mass of the transferred atom is unchanged. On the other hand, if the mass of the transferred atom differs between the isotopic reactions, transition state theory fails in the low-temperature regime ($T < 400$ K), due to the neglect of the tunneling effect.

I. Introduction

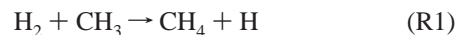
The study of reaction dynamics and kinetics is central to many areas of science. Thermal rate constants are important inputs to modeling, for instance, combustion reactions, interstellar clouds, and the atmospheres of Earth and other planets. The present work, however, does not aim to provide rate constants specifically for any of these areas; rather, the purpose is to provide accurately calculated thermal rate constants against which approximate theoretical methods can be validated and to compare with experimental results.

The reaction $\text{H} + \text{CH}_4 \rightarrow \text{CH}_3 + \text{H}_2$ has become one of the benchmarks for testing approximate theoretical dynamics calculations involving polyatomic molecules. Initially comparison was made against experimental results, but now accurately calculated thermal rate constants are available to compare with. There have been a large number of studies based on classical mechanics, reduced dimensionality quantum dynamics, and transition state theory, and we will not discuss them all here. However, we note that, employing the same potential energy surface by Jordan and Gilbert,¹ approximate rate constants have been calculated by, for instance, Yu and Nyman using a four-dimensional reduced dimensionality model (RBU),² Wang et al. using a different four-dimensional (and a five-dimensional) reduced dimensionality model (SVRT),^{3,4} Wang and Bowman using a six-dimensional reduced dimensionality model,⁵ Yang et al. using a seven-dimensional reduced dimensionality model,⁶ and Pu et al. using tunneling corrected transition state theory.⁷ Overall, the agreement between the various approaches is good, but it must also be noted that among the various reduced

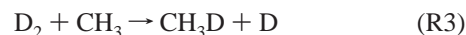
dimensionality approaches the SVRT and seven-dimensional results differ vastly from the other results, although they agree well with the experimental results.

Accurate thermal rate constants on the Jordan–Gilbert potential energy surface have been obtained using the multiconfigurational time-dependent Hartree (MCTDH) method and flux-correlation functions.^{8–10} These results show that the Jordan–Gilbert potential energy surface produces rates that are much greater than the experimental rates. Recent MCTDH calculations of thermal rate constants employing a newly developed potential energy surface based on high level ab initio calculations and Shephard interpolation produce rates that are much closer to, but lower than, the experimental results.¹¹ The accuracy of these calculations is high enough to challenge the accuracy of the experimental results.

In the present work we use the Shephard interpolated surface and the MCTDH approach to study the reverse of the $\text{H} + \text{CH}_4 \rightarrow \text{CH}_3 + \text{H}_2$ reaction and two isotopic analogues. The three reactions investigated are



and



The aim is to calculate thermal rate constants and to study the isotope effect for these three reactions and to compare the results with experimental results. The reverse of reactions R1 and R2, i.e. $\text{H} + \text{CH}_4 \rightarrow \text{CH}_3 + \text{H}_2$ and $\text{D} + \text{CH}_4 \rightarrow \text{CH}_3 + \text{HD}$, have already been studied with the MCTDH approach. Therefore, to obtain the rates of reactions R1 and R2 only requires the additional calculation of accurate reactant partition

[†] Part of the special issue "Robert E. Wyatt Festschrift".

[‡] Current address: Radboud University Nijmegen, Nijmegen, The Netherlands.

[§] Current address: Göteborg University, Göteborg, Sweden.

functions. For reaction R3, however, new quantum dynamics calculations are required and will be presented here.

It is also of general interest to know thermodynamic data for as many chemical species and reactions as possible. This facilitates finding exo- and endothermicities for unknown reactions using Hess' law. These values also give an indication of the accuracy of the ab initio calculations employed for the construction of the potential energy surface used. In this work we calculate the exo- and endothermicities of the three studied isotopically substituted reactions.

The paper is organized such that after this Introduction follows a section which describes the calculations before the results are presented and discussed. We finally draw some conclusions.

II. Theoretical Aspects

The theory employed for the rate constant calculations has been extensively described previously. Particularly relevant is the recent publication¹² on the $\text{H} + \text{CH}_4 \rightarrow \text{CH}_3 + \text{H}_2$ reaction, which we will refer to as paper I. Therefore, only the most salient features are summarized below. Some numerical details for the specific reactions studied are given in Numerical Details, together with information on how the exo- and endothermicities of these reactions were obtained.

A. Accurate Rate Constant. The thermal rate constant may be calculated from

$$k(T) = \frac{1}{2\pi\hbar[Q_r(T)]} \int dE [N_i(E)] e^{-E/k_B T} \quad (1)$$

where $N_i(E)$ is a total cumulative reaction probability. Separating out the center of mass motion of the overall system and assuming the J -shifting approximation¹³ to be valid, we can write

$$k(T) = \frac{[Q_t(T)][Q_{\text{rot}}^\ddagger(T)]}{2\pi\hbar[Q_r(T)]} \int dE [N(E)] e^{-E/k_B T} \quad (2)$$

where $Q_t(T)$ is the translational partition function of the overall system, $Q_{\text{rot}}^\ddagger(T)$ is the rotational partition function evaluated at the saddle point, and $Q_r(T)$ is the partition function of the reactants. $N(E)$ is the vibrational cumulative reaction probability for a total angular momentum $J = 0$. The J -shifting approximation¹³ is expected to be quite accurate for the present reaction, with a high barrier and quite large moments of inertia at the transition state.

In the work presented here, $N(E)$ is calculated as in paper I using

$$N(E) = \frac{e^{2(E/k_B T_0)}}{2} \sum_{f_{T_1}} \sum_{f'_{T_1}} f_{T_1} f'_{T_1} \left| \int dt e^{iEt} \langle f_{T_1} | e^{-\hat{H}(\beta_0 - \beta_1)/2} e^{-i\hat{H}t} e^{-\hat{H}(\beta_0 - \beta_1)/2} | f'_{T_1} \rangle \right|^2 \quad (3)$$

Here $\beta = 1/k_B T$, T_0 is a reference temperature, and f_{T_1} and $|f_{T_1}\rangle$ are the eigenvalues and eigenstates of the thermal flux operator

$$F_{T_1} = e^{-(\hat{H}/2k_B T_1)} \hat{F} e^{-(\hat{H}/2k_B T_1)} \quad (4)$$

where T_1 is an intermediate reference temperature, higher than T_0 . The flux operator is $\hat{F} = i[\hat{H}, h]$, where h is the Heaviside

step function, being unity on the product side and vanishing on the reactant side of a dividing surface between reactants and products. The thermal flux eigenstates appear in pairs. In each pair the states are complex conjugates of each other, one with a negative and one with a positive eigenvalue. The joint contribution of such a pair of thermal flux eigenstates is similar to the *eigen reaction probabilities* discussed in earlier work^{14,15} and will denoted here as $N_i(E)$, where $i = 0$ corresponds to the ground state contribution and $N(E) = \sum_i N_i(E)$.

To evaluate eq 3, the thermal flux operator for an imaginary time corresponding to β_1 is iteratively diagonalized to obtain the thermal flux eigenstates $|f_{T_1}\rangle$. The obtained thermal flux eigenstates $|f_{T_1}\rangle$ are thereafter propagated for the remaining imaginary time proportional to $\beta_0 - \beta_1$. Then the real time propagation is performed, and finally $N(E)$ is found according to eq 3. For the present system, the choice of $\beta_1 < \beta_0$ improved the numerical stability.

The thermal rate constant should be converged with respect to the number of thermal flux eigenstates included in $N(E)$ in eq 3. To speed up this convergence, we use the expression

$$k_n(T) = \frac{Q_{\text{rot}}^\ddagger Q_{\text{vib}}^\ddagger \sum_{i=0}^{n-1} \int e^{-E/k_B T} N_i(E) dE}{2\pi\hbar Q_r \sum_{i=0}^{n-1} e^{-(E_i - E_0)/k_B T}} \quad (5)$$

where Q_{vib}^\ddagger and Q_{rot}^\ddagger are the harmonic vibrational and rotational partition functions at the transition state and n is the number of terms in the summations in eq 5.^{16,17} When enough terms are included in eq 5, the expression for $k_n(T)$ converges to the exact rate constant $k(T)$. The reactant partition function was evaluated as accurately as possible, which is described in part C2 of section III.

B. Approximate Rate Constant. By including only one term in eq 5, we obtain an approximate rate constant. This approximation is thus based on an accurate calculation of the thermal flux contributions from the ground (vibrational) state of the activated complex and a harmonic progression for all remaining states. This means that at the transition state the ground state level is still found accurately, while all excited levels are harmonically spaced above the ground state. For consistency, the reactant partition function is therefore referenced to the accurate zero-point level but all excited-state contributions obtained in the harmonic approximation. If the relation $N_i(E + (E_i - E_0)) = N_0(E)$, where E_i is the i th vibrational level in the harmonic approximation, should hold, the exact rate constant is obtained.

If $N_0(E)$ is approximated by a step function which is zero for $E < E_b$ and unity otherwise, where E_b is the vibrationally adiabatic barrier height and the partition functions are referenced to the harmonic zero-point levels, then the transition state theory (TST) expression for $k(T)$ results:

$$k^{\text{TST}}(T) = \frac{k_B T [Q^\ddagger(T)]}{2\pi\hbar [Q_r(T)]} e^{-E_b/k_B T} \quad (6)$$

where $Q^\ddagger(T)$ is the partition function at the transition state. All TST results presented in this work employ the harmonic approximation for the vibrational partition functions (and the zero-point energies) of the reactants and of the transition state.

C. MCTDH. In MCTDH, the wave function can be represented by

$$\Psi(x_1, x_2, \dots, x_p, t) = \sum_{j_1=1}^{n_1} \dots \sum_{j_f=1}^{n_f} A_{j_1 \dots j_f}(t) \prod_{\kappa=1}^f \varphi_{j_\kappa}^\kappa(x_\kappa, t) \quad (7)$$

where $\varphi_{j_\kappa}^\kappa(x_\kappa, t)$ is a time-dependent basis function, called a single-particle function, and $A_{j_1 \dots j_f}$ is an expansion coefficient. Each single-particle function depends on a single coordinate x_κ and is represented using a time-independent (DVR or FFT) basis set $\{\chi_{i_\kappa}^\kappa(x_\kappa), i_\kappa = 1, 2, \dots, N_\kappa\}$ in that coordinate:

$$\varphi_{j_\kappa}^\kappa(x_\kappa, t) = \sum_{i_\kappa=1}^{N_\kappa} c_{j_\kappa, i_\kappa}^\kappa(t) \chi_{i_\kappa}^\kappa(x_\kappa) \quad (8)$$

Equations of motion for the expansion coefficients $A_{j_1 \dots j_f}$ and the single-particle functions $\varphi_{j_\kappa}^\kappa(x_\kappa, t)$ can be derived from the Dirac–Frenkel variational principle.^{18,19} The potential energy surface is represented by a Shepard interpolation of high-level ab initio energy points, as detailed in paper I. The potential matrix elements are calculated using the correlation DVR scheme.²⁰ An iterative, modified Lanczos diagonalization scheme²¹ is used to calculate the eigenvalues and eigenstates of the thermal flux operator.

Coordinates to be used in the MCTDH calculations should optimally render the kinetic and potential energy operators separable into terms depending on a single coordinate. In such a case there is no correlation between the coordinates and one single particle function in each coordinate would be sufficient to obtain converged results. In the present work the initial wave packet is centered at or close to the saddle point. Therefore, normal coordinates $\{Q_i\}$ are obtained at the saddle point and used to represent the wave function. This means that it is only the anharmonicity in the potential that leads to coupling between the coordinates.

In evaluating the flux operator in eq 4, it is desirable to have the Heaviside step function depend on a single coordinate. For the reactions investigated here, the obvious choice of the dividing surface at $Q_1 = 0$ was found not to be optimal.^{8,9} With this in mind, we transform two of the saddle-point normal-mode coordinates into new coordinates defined by

$$\begin{pmatrix} Q'_1 \\ Q'_j \end{pmatrix} = \begin{pmatrix} \cos \gamma & -\sin \gamma \\ \sin \gamma & \cos \gamma \end{pmatrix} \begin{pmatrix} Q_1 \\ Q_j \end{pmatrix} \quad (9)$$

where j denotes the coordinate corresponding to an X–Y–CH₃ stretch (X, Y = H/D) and γ is a rotation angle. Then a dividing surface $Q'_1 = 0$ is chosen. The optimal values of these parameters depend on which isotopic reaction is studied.

III. Numerical Details

A. Thermal Rate Constant. In this work three isotopic reactions are studied. Calculations of $N(E)$ have already been presented for the H + CH₄ → CH₃ + H₂ reaction in paper I and in ref 17 for the D + CH₄ → CH₃ + HD reaction. From these data, the rate constants for the reverse reactions can also be computed, once the corresponding reactant partition functions are known. Here we therefore only report the numerical details relevant to the D₂ + CH₃ → CH₃D + D reaction.

Convergence of the MCTDH calculations have been carefully checked, proceeding as in paper I. As for the H + CH₄ → CH₃ + H₂ reaction, the error resulting from incomplete convergence of the dynamics calculations is estimated to be below about

TABLE 1: Basis Set Parameters for the Reaction D₂ + CH₃ → CH₃D + D^a

mode	n_i	grid points	scheme
Q'_1	6	60	FFT
Q_2, Q_3	3	32	Hermite-DVR
Q_4, Q_5	3	18	Hermite-DVR
Q_6	4	48	FFT
Q'_7	4	72	FFT
Q_8, Q_9	3	8	Hermite-DVR
Q_{10}	2	8	Hermite-DVR
Q_{11}, Q_{12}	2	8	Hermite-DVR

^a n_i stands for the number of single particle functions used for the corresponding coordinate (see eqs 7–9).

10% for $k(T)$ values with $T \geq 300$ K and below about 20% for $k(T)$ values with $250 \text{ K} < T < 300 \text{ K}$. The basis set parameters used in the final production run for the reaction D₂ + CH₃ → CH₃D + D are given in Table 1. It is seen from the table that for this reaction the coordinate to be modified in eq 9 in addition to Q_1 is Q_7 . The rotation angle γ was set to $\gamma = -20^\circ$.

$Q_{\text{rot}}^\ddagger(T)$ was evaluated for a rigid rotor at the saddle point. The moments of inertia (in au) were set to 56 193, 56 193, and 21 985 for the H₂ + CH₃ → CH₄ + H reaction, to 84 032, 84 032, and 21 985 for the HD + CH₃ → CH₄ + D reaction and to 91 641, 91 641, and 21 985 for the D₂ + CH₃ → CH₃D + D reaction, all in atomic units. For CH₃ the moments of inertia were set to 22 910, 22 910, and 11 455 au.

B. Electronic Structure Calculations. We perform electronic structure calculations in the same way as described in paper I for the H + CH₄ → CH₃ + H₂ reaction.¹² In brief that means performing coupled cluster calculations using partially spin restricted CCSD(T)^{22–24} with spin restricted open-shell Hartree–Fock (RHF) reference functions. The correlation consistent polarized valence triple- ζ (cc-pVTZ) basis set was used, but with the correlation energy scaled by a factor of 1.02. In paper I this was shown to give results in good agreement with calculations using the augmented cc-pVQZ (aug-cc-pVQZ, Q = quadruple) basis set along the reaction path. It was further found in paper I that calculations using the aug-cc-pVTZ basis set and the aug-cc-pVQZ basis set give results which agree to better than 0.1 kcal/mol for the barrier height of the H + CH₄ → CH₃ + H₂ reaction. It was also shown in paper I that a single-reference method is justified. Thus, while the results would be expected to be quite accurate, we cannot be definite about the limitations resulting from the CCSD(T) approach.

C. Thermochemistry. 1. $\Delta H(T = 0 \text{ K})$. To obtain $\Delta H(T = 0)$ for the three reactions studied, we need the zero-point levels of H (D), H₂, HD, D₂, CH₃, CH₄, and CH₃D. To find the zero-point levels, we first perform electronic structure calculations to obtain energies and harmonic frequencies for the relevant species. The ab initio energies and harmonic zero-point energies we have calculated are reported in Table 2. The harmonic frequencies are given in Tables 3 and 4. To the harmonic zero-point levels we add anharmonic corrections, which are described next.

Having obtained the harmonic zero-point levels, we need the anharmonic corrections. For H₂, HD, and D₂ these were obtained using Hermite DVR calculations for increasing grid size. Required ab initio energies were calculated directly for each grid point. For CH₃ we made use of the zero-point energies obtained by Medvedev et al.²⁵ Their work is based on multi-reference configuration interaction calculations employing the aug-cc-pVTZ basis set, an accurately fitted PES, and finally Lanczos iterations to find the energy levels. Their ab initio calculations are expected to yield results very similar to ours.

TABLE 2: Energy Levels of Various Species^a

species	ab initio energy (hartrees)	harmonic ZPE (cm ⁻¹)	anharmonic cor ^b (cm ⁻¹)	ZPE (cm ⁻¹)	zero-point level (hartrees)
CH ₄	-40.442 595	9824.07	-127.8	9696.3	-40.398 415
CH ₃ D	-40.442 595	9183.76	-120.6	9063.2	-40.401 300
H	-0.499 810				-0.499 810
H ₂	-1.173 125	2202.57	-21.86	2180.7	-1.163 189
HD	-1.173 125	1907.50	-16.2	1891.3	-1.164 507
D ₂	-1.173 125	1557.49	-10.53	1547.0	-1.166 076
CH ₃	-39.764 577	6531.39	-69.1	6462.3	-39.735 133

^a See text for details. ^b Obtained as described in the text.

TABLE 3: Harmonic Frequencies (cm⁻¹) of CH₃^a

CCSD(T) VTZ 1.02 ^b	MR-CI VTZ ^c	fitted surface ^c
500.01	483	491
1424.54	1418	1421
1424.78	1418	1421
3117.25	3111	3113
3298.08	3290	3292
3298.11	3290	3292
6531.39	6505	6515

^a The last row gives the harmonic zero-point energy. ^b Present results calculated at the CCSD(T) level with a cc-pVTZ basis set and a correlation energy scaling of 1.02, as described in the text. The ab initio energy level for CH₃ is -39.764 577 hartree. ^c From Medvedev et al.²⁵ Their ab initio energy level for CH₃ is -39.764 40 hartree.

TABLE 4: Harmonic Frequencies (cm⁻¹) at the Saddle Point for HCH₄, DCH₄ and D₂CH₃, Obtained from the Potential Energy Surface^a

HCH ₄	DCH ₄	D ₂ CH ₃	CH ₄	CH ₃ D
1414.2i	1413.4i	1066.7i	1341.48	1184.84
534.0	482.6	456.3	1341.53	1184.87
534.0	482.6	456.3	1341.58	1336.04
1073.8	1006.1	886.7	1568.70	1506.10
1124.9	1104.1	886.8	1568.76	1506.17
1124.9	1104.2	992.1	3031.94	2280.62
1442.4	1393.9	1360.8	3151.34	3066.72
1442.4	1442.6	1441.3	3151.38	3151.06
1795.2	1442.9	1441.6	3151.41	3151.11
3076.3	3078.7	3078.5		
3223.3	3225.6	3225.6		
3223.3	3225.7	3225.7		

^a Also included are harmonic frequencies of CH₄ and CH₃D in cm⁻¹ calculated at the CCSD(T) level with a cc-pVTZ basis set and a correlation scaling of 1.02, as described in the text.

We calculate an anharmonic correction to our harmonic zero-point energy by using the accurate zero-point level of Medvedev et al. and their corresponding harmonic zero-point level on their potential energy surface. The anharmonic correction we find on their surface in this way is -69.1 cm⁻¹, which we add to our harmonic zero-point level. This is to bring consistency with our calculations for the other species (for H₂, HD, and D₂ we use our own harmonic zero-point levels and make anharmonic corrections to them). A comparison between our results for CH₃ and those of Medvedev et al. are given in Table 3.

For CH₄ and CH₃D we proceed in the same way as for CH₃ but use the accurate and harmonic levels of Carter et al.²⁶ to obtain an anharmonic correction, which turns out to be -127.8 cm⁻¹ for CH₄ and -120.6 cm⁻¹ for CH₃D. Our harmonic frequencies for these species are given in Table 4. The results on energy levels of the species treated here are summarized in Table 2. The resulting $\Delta H(T = 0)$ values are given in Table 5.

TABLE 5: Calculated and Experimental ΔH Values (kcal/mol)

reactn	calcd ΔH		exptl ΔH	
	$T = 0$ K	$T = 300$ K	$T = 0$ K	$T = 300$ K
H ₂ + CH ₃ → CH ₄ + H	0.06	-0.56	-0.16, ^a 0.02 ^b	-0.60 ^b
HD + CH ₃ → CH ₄ + D	0.89	0.25		
D ₂ + CH ₃ → CH ₃ D + D	0.06	-0.58		

^a From Sutherland et al.²⁷ ^b From JANAF tables.

2. $\Delta H(T = 300$ K). Table 5 contains calculated $\Delta H(T = 300$ K) values. These were obtained by assuming separability of rotational and vibrational degrees of freedom and setting

$$\Delta H(T) = \Delta H(0) + E_{\text{vib}}(\text{prod}, T) - E_{\text{vib}}(\text{react}, T) + E_{\text{rot}}(\text{prod}, T) - E_{\text{rot}}(\text{react}, T) \quad (10)$$

where $E_{\text{vib}}(\text{prod}, T)$ is the thermal vibrational energy of the products (CH₄ and CH₃D), $E_{\text{rot}}(\text{prod}, T)$ is the thermal rotational energy of the products, and “react” similarly refers to reactants. $E_{\text{vib}}(T)$ is evaluated by thermal averaging over the quantum-mechanical energy levels. For CH₃ this was done by first finding $E_{\text{vib}}(T)$ for the harmonic levels obtained from our CCSD(T)/cc-pVTZ calculations with the 1.02 correlation energy scaling and then making an anharmonic correction. This correction is given by the difference between the results obtained for $E_{\text{vib}}(T)$ using the fundamental levels and the harmonic levels on the potential energy surface of Medvedev et al.²⁵ In both cases an even energy level spacing was assumed, with the spacing being either the fundamental frequency or the harmonic frequency. The exact levels of Medvedev et al. were not used to evaluate the partition function. The reason for this is that the corresponding evaluation could not be done for CH₄, as a sufficient number of exact levels are not available. This has a negligible effect on the resulting $\Delta H(T = 300$ K) values. $E_{\text{vib}}(T)$ values for the other species were found similarly, but the anharmonic corrections for CH₄ and CH₃D were found using the fundamental and harmonic levels of Carter et al.²⁶ For H₂, HD, and D₂ we use our own harmonic and fundamental levels (though in practice these excited levels do not thermally contribute at 300 K). $E_{\text{rot}}(\text{prod}, T)$ could be safely set to $3RT/2$ for CH₃, CH₄, and CH₃D. For the diatomic molecules the rigid rotor approximation was made, and for H₂ and D₂ the existence of ortho and para forms was explicitly considered.

IV. Results and Discussion

In this section we will first discuss the results on the thermochemistry for the three reactions. These results allow a further evaluation of the accuracy of the potential energy surface employed. Then the results of the thermal rate constant calculations will be presented and discussed.

A. Thermochemistry. As far as the thermochemistry is concerned, the main results are the enthalpy changes for the three isotopic reactions at 0 and 300 K (see Table 5). For H₂ + CH₃ → CH₄ + H the calculated $\Delta H(T = 300$ K) value is -0.56 kcal/mol. The corresponding experimental value is -0.60 kcal/mol. The calculated $\Delta H(T = 0)$ value is 0.06 kcal/mol. The corresponding experimental value from the JANAF tables is 0.02 kcal/mol, while there is an updated value by Sutherland et al.²⁷ of -0.16 kcal/mol. This update would give the same change for the $\Delta H(T = 300$ K) which would then become -0.78 kcal/mol. Thus, the experimental and calculated reaction enthalpies agree to within about 0.2 kcal/mol. While the difference is slightly larger than the errors expected as a consequence of the finite basis used in the ab initio calculations ($\Delta E < 0.1$ kcal/

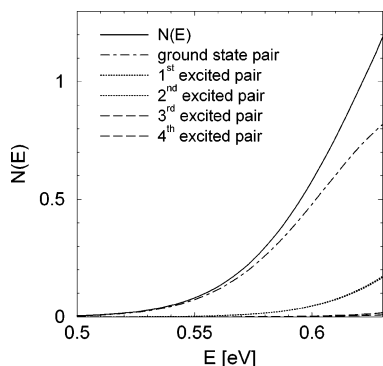


Figure 1. Cumulative reaction probability $N(E)$ (solid line) for the $\text{D}_2 + \text{CH}_3 \rightarrow \text{CH}_3\text{D} + \text{D}$ reaction as a function of energy. Contributions to $N(E)$ from individual thermal flux eigenstate pairs are also shown. The energy is referenced to the zero-point level of separated reactants.

mol), it still seems to be within the uncertainty range of the ab initio calculations when considering the limitations of the CCSD(T) approach.

For the $\text{H}_2 + \text{CH}_3 \rightarrow \text{CH}_4 + \text{H}$ reaction, we calculate an increase in exothermicity by 0.62 kcal/mol on increasing the temperature from 0 to 300 K. This is due to the thermal rotational energy of H_2 , 0.54 kcal/mol, and the thermal vibrational energy of CH_3 being 0.08 kcal/mol greater than that of CH_4 . For the $\text{HD} + \text{CH}_3 \rightarrow \text{CH}_4 + \text{D}$ and $\text{D}_2 + \text{CH}_3 \rightarrow \text{CH}_3\text{D} + \text{D}$ reactions, experimental exothermicities are not available. The calculated reaction enthalpy at 0 K for the $\text{HD} + \text{CH}_3 \rightarrow \text{CH}_4 + \text{D}$ reaction is 0.83 kcal/mol higher than for the $\text{H}_2 + \text{CH}_3 \rightarrow \text{CH}_4 + \text{H}$ reaction. This results from the lower vibrational frequency of HD compared to that of H_2 . At 300 K this difference is reduced to 0.81 kcal/mol, due to the slightly larger thermal rotational energy of HD compared to H_2 .

The reactions $\text{D}_2 + \text{CH}_3 \rightarrow \text{CH}_3\text{D} + \text{D}$ and $\text{H}_2 + \text{CH}_3 \rightarrow \text{CH}_4 + \text{H}$ have the same enthalpy change at 0 K. This is because the lower D_2 zero-point energy as compared to that of H_2 is balanced by the lower zero-point energy of CH_3D compared to CH_4 . The slight difference (0.02 kcal/mol) in reaction enthalpy between the $\text{H}_2 + \text{CH}_3 \rightarrow \text{CH}_4 + \text{H}$ and $\text{D}_2 + \text{CH}_3 \rightarrow \text{CH}_3\text{D} + \text{D}$ reactions at 300 K is due to the thermal rotational energy of D_2 being greater than that of H_2 (0.03 kcal/mol), partially offset by the slightly larger (0.01 kcal/mol) thermal vibrational energy of CH_3D compared to that of CH_4 .

B. Thermal Rate Constant. In Figure 1 cumulative reaction probabilities $N(E)$ for the $\text{D}_2 + \text{CH}_3 \rightarrow \text{CH}_3\text{D} + \text{D}$ reaction are shown as a function of energy, where the energy is referenced to the zero-point level of separated reactants. The contributions to $N(E)$ from the five lowest pairs of thermal flux eigenstates are also shown. The lowest flux eigenstate pair is nondegenerate, while the four excited pairs are doubly degenerate. It is seen that the lowest flux eigenstate pair dominates the reaction probability at energies which are important for the room-temperature rate constant. The doubly degenerate first excited thermal flux eigenstate pairs make some contribution, while higher lying flux eigenstates are of minor importance. The close degeneracy of the excited flux eigenstate contributions to $N(E)$ shows that the calculations are well converged.

In Figure 2 cumulative reaction probabilities are shown as a function of energy for each isotopic reaction. The energy is referenced to the zero-point level of separated reactants for each reaction. In the low-energy domain, the cumulative reaction probability for the $\text{D}_2 + \text{CH}_3 \rightarrow \text{CH}_3\text{D} + \text{D}$ reaction is seen to increase more slowly than the cumulative reaction probabilities for the reactions $\text{H}_2 + \text{CH}_3 \rightarrow \text{CH}_4 + \text{H}$ and $\text{HD} + \text{CH}_3 \rightarrow$

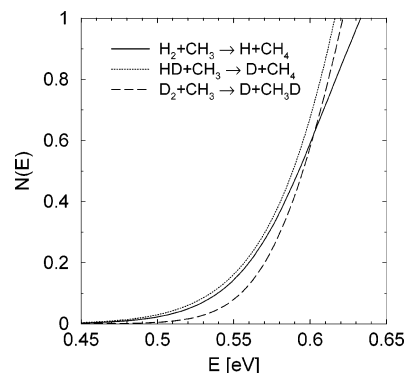


Figure 2. Cumulative reaction probabilities for the three reactions $\text{H}_2 + \text{CH}_3 \rightarrow \text{CH}_4 + \text{H}$, $\text{HD} + \text{CH}_3 \rightarrow \text{CH}_4 + \text{D}$, and $\text{D}_2 + \text{CH}_3 \rightarrow \text{CH}_3\text{D} + \text{D}$ as a function of energy. The zero of energy is the zero-point level of separated reactants. The solid line represents the reaction $\text{H}_2 + \text{CH}_3 \rightarrow \text{CH}_4 + \text{H}$, the dotted line represents the reaction $\text{HD} + \text{CH}_3 \rightarrow \text{CH}_4 + \text{D}$, and the dashed line represents the reaction $\text{D}_2 + \text{CH}_3 \rightarrow \text{CH}_3\text{D} + \text{D}$.

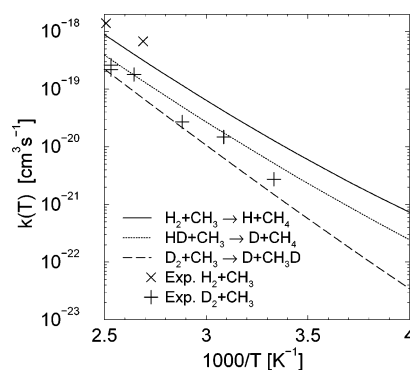


Figure 3. Accurately calculated and experimental thermal rate constants versus inverse temperature for the $\text{H}_2 + \text{CH}_3 \rightarrow \text{CH}_4 + \text{H}$, $\text{HD} + \text{CH}_3 \rightarrow \text{CH}_4 + \text{D}$, and $\text{D}_2 + \text{CH}_3 \rightarrow \text{CH}_3\text{D} + \text{D}$ reactions. Experimental values referring to the $\text{H}_2 + \text{CH}_3 \rightarrow \text{CH}_4 + \text{H}$ reaction were obtained by Shapiro and Weston²⁹ (higher temperature) and by Gesser and Steacie²⁸ (lower temperature). Experimental results for the $\text{D}_2 + \text{CH}_3 \rightarrow \text{CH}_3\text{D} + \text{D}$ reaction are from Rebbert and Steacie.³⁰

$\text{CH}_4 + \text{D}$. This is an obvious consequence of the higher mass of the transferring atom in this reaction (D versus H). This is also reflected in the lower imaginary frequency at the saddle point of the $\text{D}_2 + \text{CH}_3 \rightarrow \text{CH}_3\text{D} + \text{D}$ reaction compared to those of the $\text{H}_2 + \text{CH}_3 \rightarrow \text{CH}_4 + \text{H}$ and $\text{HD} + \text{CH}_3 \rightarrow \text{CH}_4 + \text{D}$ reactions; see Table 4. As the energy increases, the cumulative reaction probability for the $\text{D}_2 + \text{CH}_3 \rightarrow \text{CH}_3\text{D} + \text{D}$ reaction begins to increase more quickly than that of the $\text{H}_2 + \text{CH}_3 \rightarrow \text{CH}_4 + \text{H}$ reaction. This can be explained by the larger density of states at the saddle point for the $\text{D}_2 + \text{CH}_3 \rightarrow \text{CH}_3\text{D} + \text{D}$ reaction, due to the lower saddle point frequencies.

In Figure 3, the calculated thermal rate constants are shown for the three reactions studied. It is seen that the rate constant for the $\text{H}_2 + \text{CH}_3 \rightarrow \text{CH}_4 + \text{H}$ reaction is larger than that for the $\text{HD} + \text{CH}_3 \rightarrow \text{CH}_4 + \text{D}$ reaction, despite the fact that the $\text{HD} + \text{CH}_3 \rightarrow \text{CH}_4 + \text{D}$ reaction has greater cumulative reaction probabilities than the $\text{H}_2 + \text{CH}_3 \rightarrow \text{CH}_4 + \text{H}$ reaction. There are several factors giving this result. The $\text{H}_2 + \text{CH}_3 \rightarrow \text{CH}_4 + \text{H}$ reaction is favored by symmetry and by the smaller reactant translational and rotational partition functions compared to the $\text{HD} + \text{CH}_3 \rightarrow \text{CH}_4 + \text{D}$ reaction. This is only partially offset by the greater rotational and translational partition function for the $\text{HD} + \text{CH}_3 \rightarrow \text{CH}_4 + \text{D}$ reaction at the saddle point. Similar arguments explain why the $\text{D}_2 + \text{CH}_3 \rightarrow \text{CH}_3\text{D} + \text{D}$ reaction has the smallest rate constant of the three.

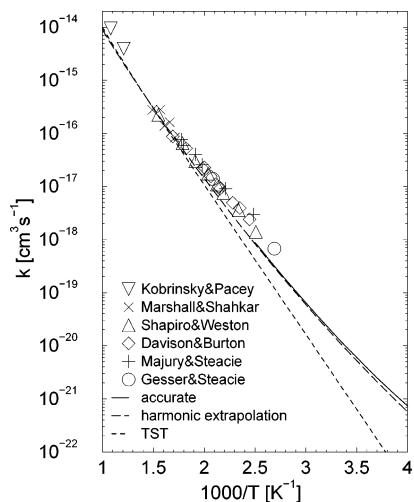


Figure 4. Accurate rate constant, harmonic extrapolation, and transition state theory rate constants for the $\text{H}_2 + \text{CH}_3 \rightarrow \text{CH}_4 + \text{H}$ reaction versus inverse temperature. The experimental values are given in refs 28, 29, and 32–35.

For the $\text{D}_2 + \text{CH}_3 \rightarrow \text{CH}_3\text{D} + \text{D}$ reaction, the vibrationally adiabatic ground state (VAG) barrier height is 13.8 kcal/mol. Thus, any reaction occurring below 13.8 kcal/mol (0.60 eV) must be attributed to tunneling, which is clearly important, as can be judged from Figure 1. By integrating $N(E)$ with a Boltzmann weighting up to 13.8 kcal/mol and comparing with the actual rate constant, obtained by integration to high energies (see eq 2), it is found that roughly 75% of the contribution to the rate constant at room temperature is due to reaction occurring below the VAG barrier height.

Figure 3 includes experimental rate constants by Gesser and Steacie²⁸ and Shapiro and Weston²⁹ for the $\text{H}_2 + \text{CH}_3 \rightarrow \text{CH}_4 + \text{H}$ reaction. The experimental rate constants are larger than the calculated values by factors of 1.6 and 2.2 for the higher and lower temperatures, respectively. Assuming an Arrhenius temperature dependence, the calculated rate constant would be in less than 35% error at these temperature if the barrier height were off by 0.3 kcal/mol. Also included in Figure 3 are experimental rate constants by Rebbert and Steacie³⁰ for the $\text{D}_2 + \text{CH}_3 \rightarrow \text{CH}_3\text{D} + \text{D}$ reaction. The differences from the accurately calculated rates are comparable to those for the $\text{H}_2 + \text{CH}_3 \rightarrow \text{CH}_4 + \text{H}$ reaction. We note that for the $\text{H} + \text{CH}_4 \rightarrow \text{CH}_3 + \text{H}_2$ reaction the difference between the most recent experimental rates and the accurately calculated rates are larger.

Figure 4 contains the accurately calculated thermal rate constant for the $\text{H}_2 + \text{CH}_3 \rightarrow \text{CH}_4 + \text{H}$ reaction and its extrapolation to higher energies using the harmonic extrapolation scheme, described in part B of section II. We refer to this approximate rate constant as $k_{\text{app}}(T)$. $k_{\text{app}}(T)$ may be viewed as a ground state tunneling corrected transition state theory rate constant. The accurately calculated thermal rate constant has been checked for convergence in the temperature range 250–400 K. There $k_{\text{app}}(T)$ agrees with the accurate rate constant to within the uncertainty range of the quantum dynamics calculations of 10–20%. The TST rate constant is seen to be smaller than $k_{\text{app}}(T)$ at temperatures below 500 K, where tunneling is important. At the higher temperatures the TST rate agrees with the extrapolated rate constants to within their uncertainties. A set of experimental results are also included in the figure. The experimental rates tend to be larger than the calculated rates.

Figure 5 corresponds to Figure 4, except for the $\text{D}_2 + \text{CH}_3 \rightarrow \text{CH}_3\text{D} + \text{D}$ reaction. The same trends as observed for the $\text{H}_2 + \text{CH}_3 \rightarrow \text{CH}_4 + \text{H}$ reaction are seen here.

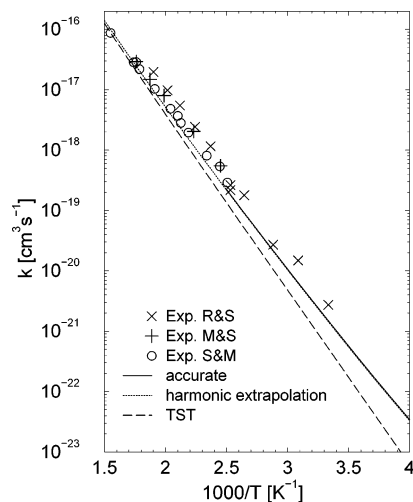


Figure 5. Accurate rate constant, harmonic extrapolation, and transition state theory rate constants for the $\text{D}_2 + \text{CH}_3 \rightarrow \text{CH}_3\text{D} + \text{D}$ reaction versus inverse temperature. The experimental values are given in refs 29, 30, and 35.

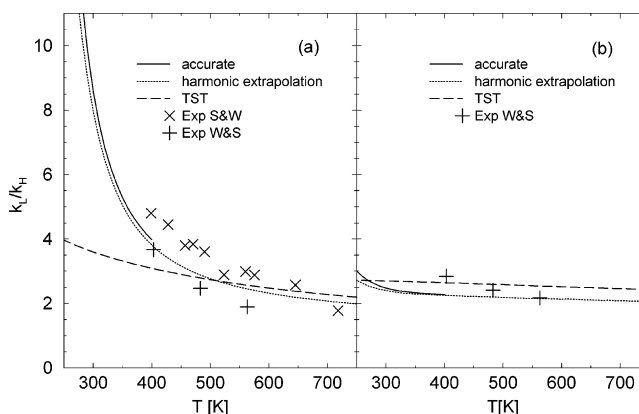


Figure 6. Kinetic isotope effect: (a) thermal rate constant for the $\text{H}_2 + \text{CH}_3 \rightarrow \text{CH}_4 + \text{H}$ reaction divided by the thermal rate constant for the $\text{D}_2 + \text{CH}_3 \rightarrow \text{CH}_3\text{D} + \text{D}$ reaction, with experimental values taken from Shapiro and Weston²⁹ (S&W) and Whittle and Steacie³¹ (W&S); (b) thermal rate constant for the $\text{H}_2 + \text{CH}_3 \rightarrow \text{CH}_4 + \text{H}$ reaction divided by the thermal rate constant for the $\text{HD} + \text{CH}_3 \rightarrow \text{CH}_4 + \text{D}$ reaction, with experimental values taken from Whittle and Steacie³¹ (W&S).

In Figure 6 kinetic isotope effects are shown. The kinetic isotope effect (KIE) is calculated as the thermal rate for the reaction with the light isotope divided by the thermal rate for the reaction with the heavier isotope. The left-hand panel shows the KIE for the rate of the reaction $\text{H}_2 + \text{CH}_3 \rightarrow \text{CH}_4 + \text{H}$ compared to that of $\text{D}_2 + \text{CH}_3 \rightarrow \text{CH}_3\text{D} + \text{D}$. Calculated results and experimental results by Shapiro and Weston²⁹ and Whittle and Steacie³¹ have been included. The right-hand panel shows the calculated KIE for the rate of the $\text{H}_2 + \text{CH}_3 \rightarrow \text{CH}_4 + \text{H}$ reaction compared to that of the $\text{HD} + \text{CH}_3 \rightarrow \text{CH}_4 + \text{D}$ reaction and experimental results by Whittle and Steacie.³¹

Experimental kinetic isotope effects are expected to be more accurate than the individual rate constants which make up the ratio. This is due to cancellation of errors, such as possible errors in the rate of a reference reaction. With regard to the accuracy of the calculated KIE effect, there are two points to consider. First, the effect of errors in the potential energy surface is reduced, resulting in increased accuracy. Second, uncertainties resulting from the MCTDH procedure remain for each reaction and are uncorrelated between the reactions, thus contributing to larger uncertainties for the KIE.

Looking at Figure 6, we find that the experimental KIE and the KIE calculated from quantum dynamics for the H₂ + CH₃ → CH₄ + H reaction compared with the D₂ + CH₃ → CH₃D + D reaction agree to within 25% for every data point. The agreement is similar for the KIE for the H₂ + CH₃ → CH₄ + H reaction compared to the HD + CH₃ → CH₄ + D reaction. The experimental kinetic isotope effects are considered to agree with the quantum dynamically based ones to within the estimated uncertainty. It is noted that there is hardly any temperature dependence in the KIE when the mass of the transferred atom is the same in both isotopic reactions (as for the H₂ + CH₃ → CH₄ + H and HD + CH₃ → CH₄ + D reactions).

TST underestimates the KIE below 400 K in the case when the mass of the transferring atom is different between the two isotopic reactions. This is to be expected, as tunneling is not considered, which becomes increasingly important as the temperature is lowered and more so for the light isotope. At higher temperatures and for the case when the mass of the transferred atom is unchanged between the isotopic reactions, the KIE calculated with TST agrees with the other results to within the estimated uncertainty.

V. Conclusions

Accurate quantum-mechanical results for thermodynamic data, cumulative reaction probabilities (for $J = 0$), and thermal rate constants of the three isotopic reactions H₂ + CH₃ → CH₄ + H, HD + CH₃ → CH₄ + D, and D₂ + CH₃ → CH₃D + D have been presented. The calculations were performed using flux correlation functions and the multiconfigurational time-dependent Hartree (MCTDH) method to propagate wave packets employing a high-level Shephard interpolated potential energy surface based on high-level ab initio calculations.

For the H₂ + CH₃ → CH₄ + H and D₂ + CH₃ → CH₃D + D reactions, experimental rate constants from several groups are available. In comparing to these, we typically find agreement to within a factor of 2. The kinetic isotope effects for the rate of the H₂ + CH₃ → CH₄ + H reaction compared to those for the HD + CH₃ → CH₄ + D and D₂ + CH₃ → CH₃D + D reactions have also been calculated and found to agree with experimental results to within 25% for all data points. The calculated exothermicity for the H₂ + CH₃ → CH₄ + H reaction agrees to within 0.2 kcal/mol with experimentally deduced values.

For kinetic isotope effects, TST was found to be accurate if the mass of the transferring atom is unchanged (“secondary isotope effect”). If the mass differs (“primary isotope effect”),

differences between the accurate results and the TST ones are found at lower temperatures where tunneling is important.

Acknowledgment. We are grateful to Professor Phil Pacey for supplying us with the experimental rate data. Financial support by the Deutsche Forschungsgemeinschaft, the Swedish Research Council, and the Fond der Chemischen Industrie is gratefully acknowledged.

References and Notes

- (1) Jordan, M.; Gilbert, R. *J. Chem. Phys.* **1995**, *102*, 5669.
- (2) Yu, H.-G.; Nyman, G. *J. Chem. Phys.* **1999**, *111*, 3508.
- (3) Wang, M.; Li, Y.; Zhang, J.; Zhang, D. *J. Chem. Phys.* **2000**, *113*, 1802.
- (4) Wang, M.; Zhang, J. *J. Chem. Phys.* **2002**, *117*, 3081.
- (5) Wang, D.; Bowman, J. *J. Chem. Phys.* **2001**, *115*, 2055.
- (6) Yang, M.; Zhang, D. H.; Lee, S.-Y. *J. Chem. Phys.* **2002**, *117*, 9539.
- (7) Pu, J.; Corchado, J.; Truhlar, D. *J. Chem. Phys.* **2001**, *115*, 6266.
- (8) Huarte-Larranaga, F.; Manthe, U. *J. Chem. Phys.* **2000**, *113*, 5115.
- (9) Huarte-Larranaga, F.; Manthe, U. *J. Phys. Chem. A* **2001**, *105*, 2522.
- (10) Huarte-Larranaga, F.; Manthe, U. *J. Chem. Phys.* **2002**, *116*, 2863.
- (11) Wu, T.; Werner, H.; Manthe, U. *Science* **2004**, *306*, 2227.
- (12) Wu, T.; Werner, H.-J.; Manthe, U. *J. Chem. Phys.* **2006**, *124*, 164306.
- (13) Bowman, J. M. *J. Phys. Chem.* **1991**, *95*, 4960.
- (14) Manthe, U.; Miller, W. H. *J. Chem. Phys.* **1993**, *99*, 3411.
- (15) Manthe, U.; Matzkies, F. *Chem. Phys. Lett.* **1998**, *282*, 442.
- (16) Huarte-Larranaga, F.; Manthe, U. *J. Chem. Phys.* **2002**, *117*, 4635.
- (17) van Harrevelt, R.; Nyman, G.; Manthe, U. *J. Chem. Phys.* **2007**, *126*, 084303.
- (18) Meyer, H.-D.; Manthe, U.; Cederbaum, L. S. *Chem. Phys. Lett.* **1990**, *165*, 73.
- (19) Manthe, U.; Meyer, H.-D.; Cederbaum, L. S. *J. Chem. Phys.* **1992**, *97*, 3199.
- (20) Manthe, U. *J. Chem. Phys.* **1996**, *105*, 6989.
- (21) Manthe, U.; Matzkies, F. *Chem. Phys. Lett.* **1996**, *252*, 7.
- (22) Knowles, P. J.; Hampel, C.; Werner, H.-J. *J. Chem. Phys.* **1993**, *99*, 5219.
- (23) Knowles, P. J.; Hampel, C.; Werner, H.-J. *J. Chem. Phys.* **2000**, *112*, 3106.
- (24) Deegan, M. J. O.; Knowles, P. J. *Chem. Phys. Lett.* **1994**, *227*, 321.
- (25) Medvedev, D. M.; Harding, L. B.; Gray, S. K. *Mol. Phys.* **2006**, *104*, 73.
- (26) Carter, S.; Shnider, H. M.; Bowman, J. M. *J. Chem. Phys.* **1999**, *110*, 8417.
- (27) Sutherland, J. W.; Su, M.-C.; Michael, J. V. *Int. J. Chem. Kinet.* **2001**, *33*, 669.
- (28) Gesser, H.; Steacie, E. W. R. *Can. J. Chem.* **1956**, *34*, 113.
- (29) Shapiro, J. S.; Weston, R. E. *J. Phys. Chem.* **1972**, *76*, 1669.
- (30) Rebbert, R. E.; Steacie, E. W. R. *Can. J. Chem.* **1954**, *32*, 113.
- (31) Whittle, R. E.; Steacie, E. W. R. *J. Chem. Phys.* **1953**, *21*, 993.
- (32) Kobrinsky, P. C.; Pacey, P. D. *Can. J. Chem.* **1974**, *52*, 3665.
- (33) Marshall, R. M.; Shakhar, G. *J. Chem. Soc., Faraday Trans. 1* **1981**, *77*, 2271.
- (34) Davison, S.; Burton, M. *J. Am. Chem. Soc.* **1952**, *74*, 2307.
- (35) Majury, T. G.; Steacie, E. W. R. *Can. J. Chem.* **1952**, *30*, 800.